Nano-Micro Letters

ISSN 2311-6706
e-ISSN 2150-5551
CN 31-2103/TB

ARTICLE

https://doi.org/10.1007/s40820-019-0339-0

Cite as
Nano-Micro Lett.
(2020) 12:6

Received: 30 September 2019
Accepted: 20 November 2019

Photocatalytic H_2 Evolution on TiO_2 Assembled with Ti_3C_2 MXene and Metallic 1T-WS_2 as Co-catalysts

Yujie Li[1], Lei Ding[1], Shujun Yin[1], Zhangqian Liang[1], Yanjun Xue[1], Xinzhen Wang[1] ✉, Hongzhi Cui[1] ✉, Jian Tian[1] ✉

Yujie Li and Lei Ding have contributed equally to this work.

✉ Xinzhen Wang, xzwang@sdust.edu.cn; Hongzhi Cui, cuihongzhi1965@163.com; Jian Tian, jiantian@sdust.edu.cn

[1] School of Materials Science and Engineering, Shandong University of Science and Technology, Qingdao 266590, People's Republic of China

HIGHLIGHTS

- The 1T-WS_2@TiO_2@Ti_3C_2 photocatalyst is highly active for water splitting to produce hydrogen at 3409.8 μmol g^{-1} h^{-1}.
- The Ti_3C_2 MXene and octahedral (1T) phase WS_2 act pathways transferring photogenerated electrons.

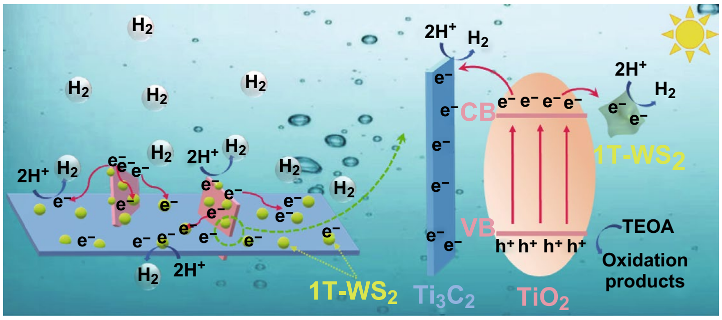

ABSTRACT The biggest challenging issue in photocatalysis is efficient separation of the photoinduced carriers and the aggregation of photoexcited electrons on photocatalyst's surface. In this paper, we report that double metallic co-catalysts Ti_3C_2 MXene and metallic octahedral (1T) phase tungsten disulfide (WS_2) act pathways transferring photoexcited electrons in assisting the photocatalytic H_2 evolution. TiO_2 nanosheets were in situ grown on highly conductive Ti_3C_2 MXenes and 1T-WS_2 nanoparticles were then uniformly distributed on TiO_2@Ti_3C_2 composite. Thus, a distinctive 1T-WS_2@TiO_2@Ti_3C_2 composite with double metallic co-catalysts was achieved, and the content of 1T phase reaches 73%. The photocatalytic H_2 evolution performance of 1T-WS_2@TiO_2@Ti_3C_2 composite with an optimized 15 wt% WS_2 ratio is nearly 50 times higher than that of TiO_2 nanosheets because of conductive Ti_3C_2 MXene and 1T-WS_2 resulting in the increase of electron transfer efficiency. Besides, the 1T-WS_2 on the surface of TiO_2@Ti_3C_2 composite enhances the Brunauer–Emmett–Teller surface area and boosts the density of active site.

KEYWORDS Photocatalytic H_2 production; Ti_3C_2 MXene; Octahedral phase WS_2; TiO_2 nanosheets; Co-catalysts

1 Introduction

Due to energy consumption and consequent environmental pollution, the generation of hydrogen (H_2) from water using solar light through semiconductors materials has aroused great attention [1–4]. Among these, TiO_2 is widely studied owing to nontoxicity and low cost [5, 6]. However, the fast photoexcited carrier recombination restricts the TiO_2's application, and thus numerous efforts, such as doping, co-catalyst loading and heterostructure designing, are made to improve photoexcited carrier separation [7, 8]. Among these, co-catalysts can gather carriers to improve separation and act as active sites for H_2 production [9]. Noble metals as excellent co-catalysts have widely applied to photocatalysis. However, extreme scarcity and high price restrict their application of photocatalytic water splitting [10, 11]. Therefore, seeking an inexpensive and highly active co-catalyst is of paramount significance for achieving photocatalytic H_2 production in the future [12].

MXenes, as new 2D materials, have aroused remarkable attention because of its excellent electrical conductivity [13, 14]. For example, a 2D material with an accordion-like structure of layered Ti_3C_2 MXene can be prepared by etching Al layers from Ti_3AlC_2, in HF solution [15–17]. Due to its high electrical conductivity and unique layer morphology, Ti_3C_2 MXene is an appropriate substitute co-catalyst for noble metals for photocatalytic H_2 evolution [18].

In recent years, transition metal disulfides (TMDs), such as molybdenum disulfide (MoS_2) and tungsten disulfide (WS_2), are regarded as promising substitutes for noble metals on catalysis [19, 20]. MoS_2 and WS_2 mainly include semiconductive trigonal (2H) phase and metallic octahedral (1T) phase [21, 22]. Both experimental and theoretical research have revealed that the metallic 1T phase possesses outstanding conductivity and more active sites, which will be suitable co-catalyst for photocatalytic H_2 evolution, compared with 2H phase [23]. As one of the most popular TMDs materials, 1T phase MoS_2 has been widely studied on photocatalysis [24–26]. However, the report about 1T phase WS_2 (1T-WS_2) on photocatalytic H_2 production is still rare.

In this paper, an innovative 2D heterojunction by utilizing the metallic feature of Ti_3C_2 MXene and 1T-WS_2 is reported. A two-step hydrothermal method is used for designing the novel 1T-WS_2@TiO_2@Ti_3C_2 photocatalyst where Ti_3C_2 MXene and 1TWS_2 play important roles as electron acceptors. Firstly, TiO_2 nanosheets are in situ grown on the surface of highly conductive Ti_3C_2 MXenes to construct TiO_2@Ti_3C_2 composites by a facile hydrothermal method. Secondly, we intentionally employ the 1T-WS_2 nanoparticles evenly distribute on TiO_2@Ti_3C_2 composites' surface using a hydrothermal process. This procedure results in the construction of an efficient photocatalytic system with intimate contact among metallic Ti_3C_2 MXene, 1T-WS_2 nanoparticles, and TiO_2 NSs. The newly designed 1T-WS_2@TiO_2@Ti_3C_2 composites exhibit extremely enhanced photocatalytic H_2 evolution activity and stability owing to the novel structure.

2 Experimental Procedures

2.1 Materials

Ti_3AlC_2 powder was purchased from 11 Technology. Hydrochloric acid (HCl), sodium tetrafluoroborate ($NaBF_4$), hydrofluoric acid (HF, 40 wt%), tungsten chloride (WCl_6), thioacetamide (TAA), and dimethylformamide (DMF) were provided by Sinopharm.

2.2 Synthesis of Ti_3C_2 MXenes

In a typical synthesis, 1 g Ti_3AlC_2 powders were dissolved in 120 mL HF solution (40 wt%) and were stirred for 72 h. Then, the mixed solution was washed with deionized (DI) water to neutral. Lastly, Ti_3C_2 MXenes were dried at 50 °C for overnight in a vacuum oven.

2.3 Synthesis of TiO_2@Ti_3C_2 Composites

Ti_3C_2 MXenes (400 mg) and $NaBF_4$ (660 mg) were dissolved in 60 mL HCl (1.0 M) and were stirred for 30 min. The mixed solution was hydrothermally treated at 160 °C for 12 h. The obtained TiO_2@Ti_3C_2 composites were washed with DI water and dried at 60 °C for overnight in a vacuum oven.

2.4 Synthesis of 1T-WS_2@TiO_2@Ti_3C_2 Composites

WCl_6 (24 mg) and TAA (9 mg) were added into 50 mL DMF. Then, 100 mg TiO_2@Ti_3C_2 composites were dispersed in above solution and were stirred for 60 min. The mixed solution was hydrothermally treated at 200 °C for 24 h. The obtained 1T-WS_2@TiO_2@Ti_3C_2 composites (15 wt% WS_2) were washed with DI water and dried at 60 °C for overnight in a vacuum oven. By adjusting the adding amount of WCl_6 (16, 32, and 40 mg) and TAA (6, 12, and 15 mg), 1T-WS_2@TiO_2@Ti_3C_2 composites with other WS_2 adding amounts (10, 20, and 25 wt%) were prepared, respectively.

2.5 Characterizations

The phases of the samples were carried out using D/Max 2500PC X-ray diffraction (XRD). The surface characteristic and structure of the samples were tested by a FEI Nano 450 high-resolution scanning electron microscope (FESEM) and a JEOL 2100F high transmission electron microscope (HRTEM). The chemical states of the products were analyzed by a Thermo ESCALAB 250XI X-ray photoelectron spectrometry (XPS). The specific surface area and pore size distribution were tested by a nitrogen adsorption–desorption apparatus (Micromeritics ASAP2020) using the Brunauer–Emmett–Teller (BET) method. The UV–Vis diffuse reflectance spectra (DRS) of the products were measured using a Hitachi UH3101 UV–Vis spectrophotometer. The photoluminescence (PL) spectra were tested by a FLS920 fluorescence.

2.6 Photoelectrochemical and Photocatalytic Activity Test

The photocatalytic activity test was measured using a Pyrex glass vessel, with a 300 W Xe arc lamp (CELHXF300) with an AM-1.5 filter as the light source. 10 mg of catalysts were added into acetone/TEOA solution (15 mL acetone + 5 mL TEOA + 80 mL DI water). The amount of generated H_2 was tested by a gas chromatograph (Techcomp GC-7920). The electrochemical impedance spectroscopy (EIS) and transient photocurrent response (PEC) of the catalysts were measured by an electrochemical workstation (CHI660D) under a 300 W Xe arc lamp with an AM-1.5 filter in a three-electrode cell (0.5 M Na_2SO_4). Ag/AgCl electrode and Pt wire were used as reference and counter electrodes, respectively.

3 Results and Discussion

A typical synthesis route of 1T-WS_2@TiO_2@Ti_3C_2 composites is schematically depicted in Scheme 1. Ti_3C_2 MXenes are firstly prepared by etching Al layers of Ti_3AlC_2 MAX phase in HF solution [27]. Then, the layered Ti_3C_2 MXene provides Ti sources with the help of HCl and $NaBF_4$ for growing TiO_2 NSs across the layered Ti_3C_2 MXene. Finally, the obtained TiO_2@Ti_3C_2 composites are added into WCl_6/TAA solutions at 200 °C for 24 h to introduce 1T-WS_2 co-catalysts. In this process, due to the intercalation of NH_4^+ of TAA, the space distance of WS_2 increases and 1T-WS_2 is generated [19]. The 1T-WS_2 is evenly assembled on TiO_2@Ti_3C_2 composites' surface to construct the ternary 1T-WS_2@TiO_2@Ti_3C_2 composites.

After HF etching, the most intense XRD (104) peak of Ti_3AlC_2 was disappeared, and the (002) peak of Ti_3AlC_2 at 9.52° was moved to lower 2-theta value (8.78°), which indicates the successful formation of Ti_3C_2 (Fig. S1a) [17]. The development of TiO_2 nanosheets across Ti_3C_2 MXenes by the hydrothermal oxidation of Ti_3C_2 is evidenced by the emergence of diffraction peaks of anatase TiO_2 (JCPDS No.

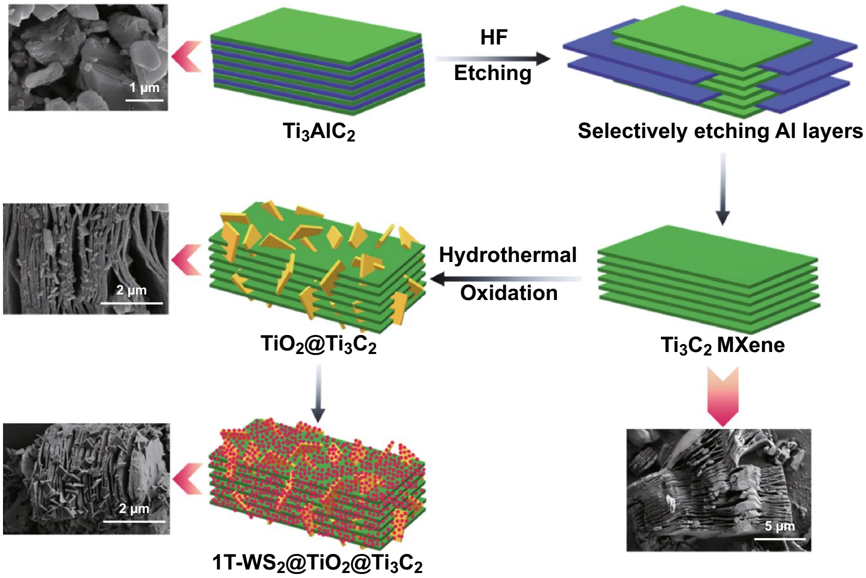

Scheme 1 Schematic illustration of the preparation of 1T-WS_2@TiO_2@Ti_3C_2 composites

21-1272) as shown in Fig. 1a. The XRD peaks appearing at 6.66°, 13.40°, and 20.10° are indexed to (002), (004), and (006) planes of 1T-WS_2 [23]. The co-existence of Ti_3C_2, TiO_2, and 1T-WS_2 indicates the successful preparation of 1T-WS_2@TiO_2@Ti_3C_2 composites. For 1T-WS_2@TiO_2@Ti_3C_2 composites with other WS_2 ratios (Fig. S1b), all the XRD peaks are well corresponding to Ti_3C_2, TiO_2, or 1T-WS_2.

The full-scale XPS spectrum of 1T-WS_2@TiO_2@Ti_3C_2 composites (Fig. 1b) displays that Ti, C, O, S, and W are dominant elements, while F element is ascribed to F^- ions physically adsorbed on composites from the HF solution. The Ti 2*p* spectrum is divided into four peaks (Fig. 1c). The two peaks at 464.7 (Ti–O $2p_{1/2}$) and 459.0 eV (Ti–O $2p_{3/2}$) are ascribed to lattice Ti–O bonds of TiO_2 [28]. The other two peaks at 461.2 (Ti-C $2p_{1/2}$) and 455.3 eV (Ti-C $2p_{3/2}$) are indexed to lattice Ti–C bonds of Ti_3C_2 [29]. The high-resolution Ti 2*p* XPS spectrum indicates the content of Ti_3C_2 is about 79% in TiO_2@Ti_3C_2 composites. The W 4*f* XPS spectrum of 1T-WS_2@TiO_2@Ti_3C_2 composites (Fig. 1d) can confirm the presence and relative content of 1T-WS_2. In the W 4*f* region, the two peaks of 2H phase corresponding to W $4f_{7/2}$ and W $4f_{5/2}$ at 33.0 and 36.0 eV, respectively. Nevertheless, two extra peaks shift to lower binding energies at 32.4 and 34.6 eV, suggesting the existence of 1T-WS_2 [19, 30]. The 1T phase content is calculated about 73%, which shows that the 1T-WS_2@TiO_2@Ti_3C_2 composites are composed of lots of metallic 1T phase.

Ti_3C_2 MXenes are obtained by etching of the aluminum layer of the bulk Ti_3AlC_2 (Fig. S2a) by using HF. As shown in Fig. 2a, Ti_3C_2 MXenes present typical accordion-like multilayer structure. After hydrothermal oxidation of Ti_3C_2 MXenes, the layered Ti_3C_2 MXenes provide Ti sources for growing TiO_2 NSs inserting across the layered Ti_3C_2 MXene to form TiO_2@Ti_3C_2 composites, and further combine with WS_2 through hydrothermal reaction to get 1T-WS_2@TiO_2@Ti_3C_2 composites. Figure 2b shows that 1T-WS_2 presents nanoflake structures and agglomerate into nanoflowers. After combining with TiO_2@Ti_3C_2 composites, the 1T-WS_2 nanoparticles are evenly distributed on TiO_2@Ti_3C_2 composites' surface (Fig. 2c, d). Furthermore, 1T-WS_2@TiO_2@Ti_3C_2 composites with other WS_2 ratios (10, 20, and 25 wt%)

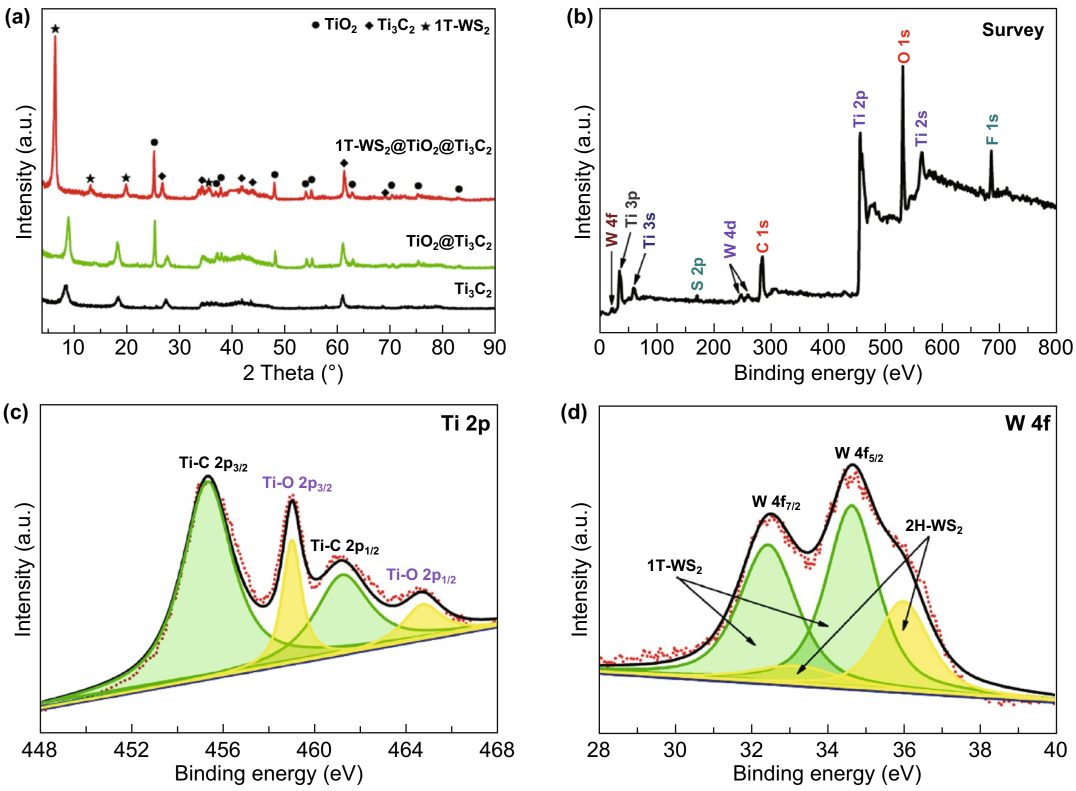

Fig. 1 **a** XRD patterns of Ti_3C_2, TiO_2@Ti_3C_2, and 1T-WS_2@TiO_2@Ti_3C_2 composites (15 wt% WS_2); **b** fully scanned XPS spectrum, **c** Ti 2*p*, and **d** W 4*f* XPS spectra in 1T-WS_2@TiO_2@Ti_3C_2 composites (15 wt% WS_2)

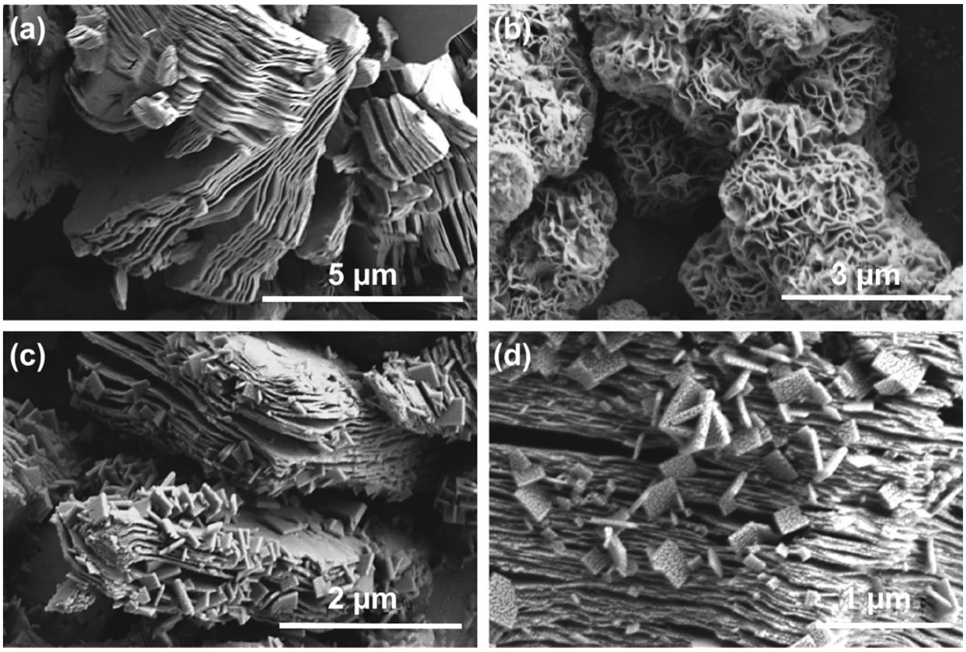

Fig. 2 SEM images of **a** Ti_3C_2 MXene, **b** 1T-WS_2, and **c, d** 1T-WS_2@TiO_2@Ti_3C_2 composites (15 wt% WS_2)

are prepared, and corresponding SEM images are displayed in Fig. S2.

The phase composition and microscopic structure of 1T-WS_2@TiO_2@Ti_3C_2 composites are characterized by TEM (Fig. 3a, b). The lattice with *d* spaces of 0.35 nm is attributed to (101) plane of anatase TiO_2 (Fig. 3b), which are same as the description of the literatures [31, 32]. The lattice spacings of 0.98 and 0.92 nm are indexed to (002) plane of Ti_3C_2 MXene and (002) plane of 1T-WS_2 [19, 33–35] (Fig. 3b). The EDX element mappings of composites (Fig. 3c) indicate that the Ti, C, O, W, and S elements are accordantly distributed. The as-fabricated photocatalyst with superior metallic quality of Ti_3C_2 MXene and 1T-WS_2 present more effective carrier transfer and separation compared with TiO_2 NSs, and therefore, the photocatalytic performance is enhanced. The 1T-WS_2 is further confirmed by

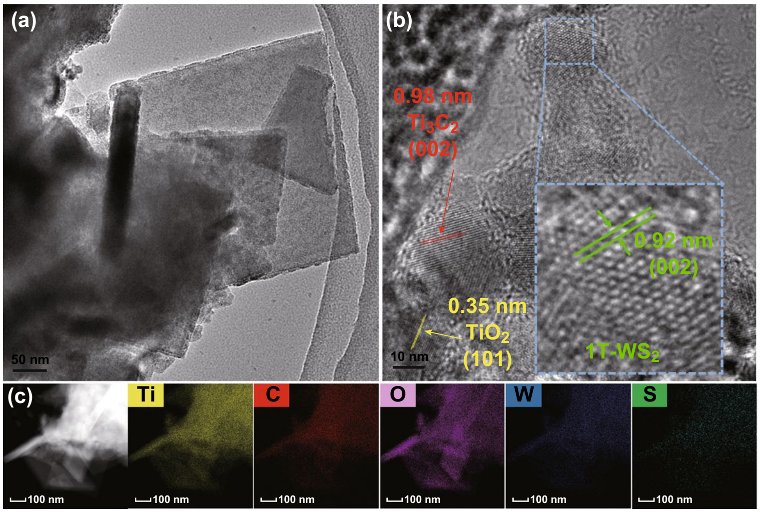

Fig. 3 **a**, **b** HRTEM and **c** EDX elemental mapping images of 1T-WS_2@TiO_2@Ti_3C_2 composites (15 wt% WS_2)

Raman spectroscopy (Fig. S3). Remarkably, in contrast to 2H phase WS_2, there are no scattering peaks between 350 and 450 cm^{-1} attributed to E^1_{2g} (in-plane) and A_{1g} (out-of-plane) in 1T-WS_2 (Fig. S3). There are also two strong peaks at low frequency range for 1T-WS_2. One strong Raman band at 128 cm^{-1} (J_1) is attributed to W–W stretching vibrations in 1T-WS_2@TiO_2@Ti_3C_2 composite [21]. Besides, another additional peak at 171 cm^{-1} (J_2) is observed, which is associated with the phonon modes in the WS_2, suggesting the existence of a considerable amount of 1T phase ingredient embedded [22]. This result further implies that the as-prepared WS_2 in 1T-WS_2@TiO_2@Ti_3C_2 composites is mostly 1T phase [19, 23].

To further examine the textural properties of 1T-WS_2@TiO_2@Ti_3C_2 composites, the isotherms and the pore size distributions are studied by N_2 adsorption–desorption measurement (Figs. 4 and S4). All of samples present type IV isotherms with H3 hysteresis loops, suggesting the presence of mesopores [36]. And the pore size distribution curves of 1T-WS_2@TiO_2@Ti_3C_2 composites with different WS_2 loading amounts (Fig. 4a–d inset) display that the size of major mesopores ranges from 2 to 25 nm. Compared with other samples, when the loading amount of WS_2 is 15%, the pore size distribution is relatively concentrated at 2 ~ 5 nm. The presence of such a small pore size is conducive to migration of reactant and product molecules to facilitate photocatalytic reactions. Moreover, larger nitrogen adsorption capacity indicates that more reactive sites may be provided during the reaction process, which is favorable in the enhancement of catalytic activity. The BET surface area of as-prepared 1T-WS_2@TiO_2@Ti_3C_2-15%, as shown in Table S1, reveals a higher surface area (23.334 m^2 g^{-1}) than those of Ti_3C_2 MXene, pure 1T-WS_2, and 1T-WS_2@TiO_2@Ti_3C_2 composites with other WS_2 loading amounts. In addition, as shown in Figs. 4 and S4, the BET surface area of the samples increase nonlinearly with increasing WS_2 loading. As the WS_2 loading amount increases from 10 to 15 wt%, the BET surface area of composites increases. However, further

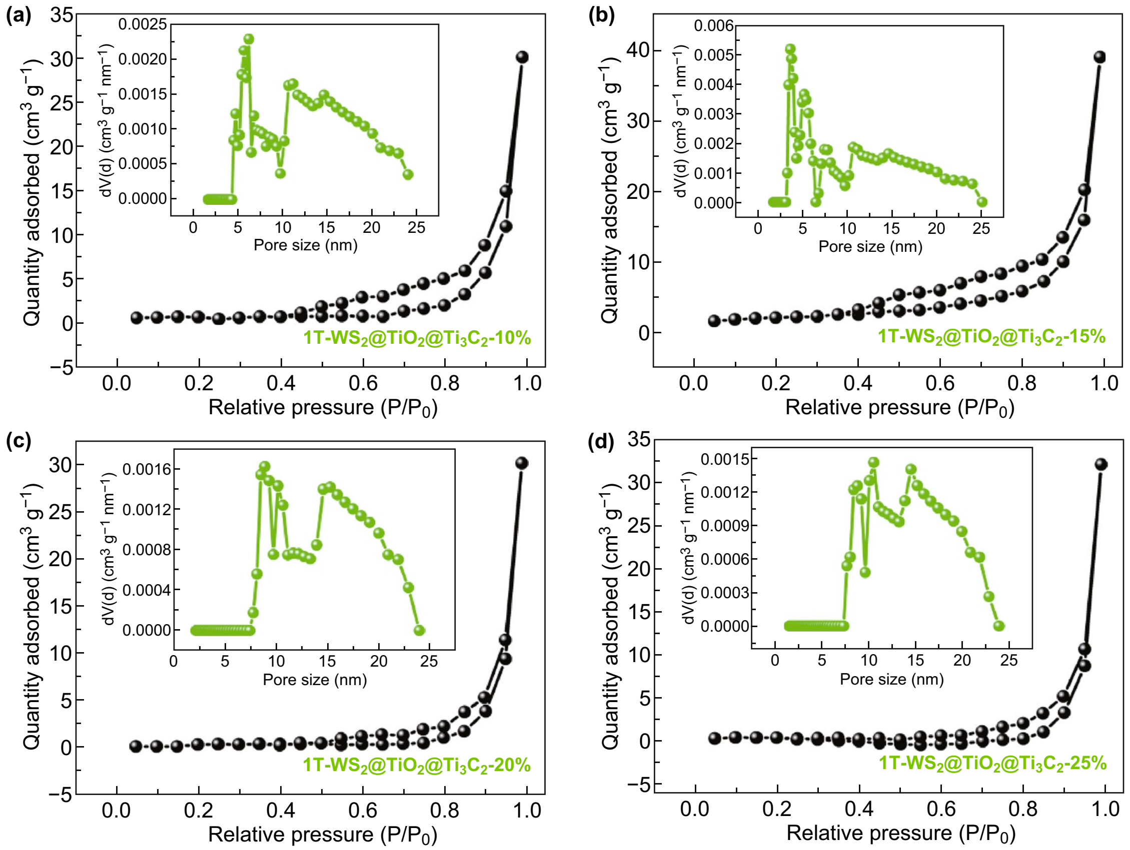

Fig. 4 N_2 adsorption–desorption isotherms and corresponding pore size distribution curves (inset) of 1T-WS_2@TiO_2@Ti_3C_2 composites with **a** 10 wt%, **b** 15 wt%, **c** 20 wt%, and **d** 25 wt% WS_2 ratios

https://doi.org/10.1007/s40820-019-0339-0

increasing the loading amount of WS_2 (from 15 to 25 wt% WS_2) leads to a gradual decrease of BET surface area, which may be caused by the aggregation of WS_2 on the surface of the composites. The higher surface areas are beneficial for photocatalysis since it could provide more adsorption and active sites, thus the photocatalytic activity is improved [37].

To investigate the optical absorptivity, the UV–Vis DRS spectra of samples are measured. As shown in Fig. 5, TiO_2 NSs (curve black) have a noticeable UV light absorption, due to the nature of anatase TiO_2 [38]. Ti_3C_2 MXene (curve blue) shows UV and visible absorption as a result of the black color nature [39]. Compared with TiO_2 NSs, 1T-WS_2@TiO_2@Ti_3C_2 composites (15 wt% WS_2) display a significant absorption edge red shift and enhanced visible absorption, which is attributed to the optical absorption of Ti_3C_2 MXene and 1T-WS_2. The increase of light absorption range of photocatalysts will be more helpful to promote the progress of photocatalytic reaction. Besides, the 1T-WS_2@TiO_2@Ti_3C_2 composites show stronger light absorption with the increase of WS_2 contents from 10 to 25 wt% (Fig. S5).

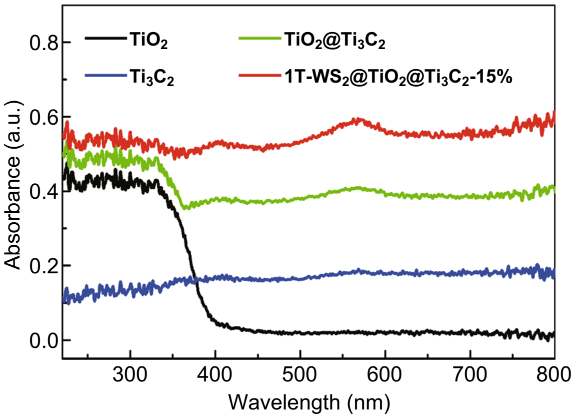

Fig. 5 UV–Vis DRS spectra of Ti_3C_2 MXene, TiO_2 NSs, TiO_2@Ti_3C_2, and 1T-WS_2@TiO_2@Ti_3C_2 composites (15 wt% WS_2)

The photocatalytic performance of 1T-WS_2@TiO_2@Ti_3C_2 composites was evaluated using H_2 evolution under simulated sunlight irradiation in an aqueous acetone solution at room temperature (Fig. 6). Control experiments (Fig. S6) show that no noticeable H_2 evolution is discovered without either photocatalyst or illumination. TiO_2 NSs (Fig. 6) present limited photocatalytic H_2 activity (67.8 μmol g^{-1} h^{-1}), arising from fast carrier recombination [40]. In view of the excellent electronic conductivity of Ti_3C_2 and 1T-WS_2, it is combined as a co-catalyst with TiO_2 NSs in order to achieve better photogenerated carrier separation and improve photocatalytic performance [41, 42]. As expected, after assembling of Ti_3C_2 and 1T-WS_2, the bets photocatalytic activity is detected (3409.8 μmol g^{-1} h^{-1} for 1T-WS_2@TiO_2@Ti_3C_2 composites (15 wt% WS_2)), which is nearly 50 times higher than that of TiO_2 NSs. Moreover, the 1T-WS_2@TiO_2@Ti_3C_2 composites (10 wt% WS_2) present a lower photocatalytic activity than 1T-WS_2@TiO_2@Ti_3C_2 composites (15 wt% WS_2), owing to the relatively weaker solar light input. Furthermore, with the increase of WS_2 contents from 15 to 25 wt%, a reduction in the photocatalytic performance of 1T-WS_2@TiO_2@Ti_3C_2 composites is discovered. Because excess black 1T-WS_2 nanoparticles induced "shielding effect" block light to the surface of TiO_2 [43].

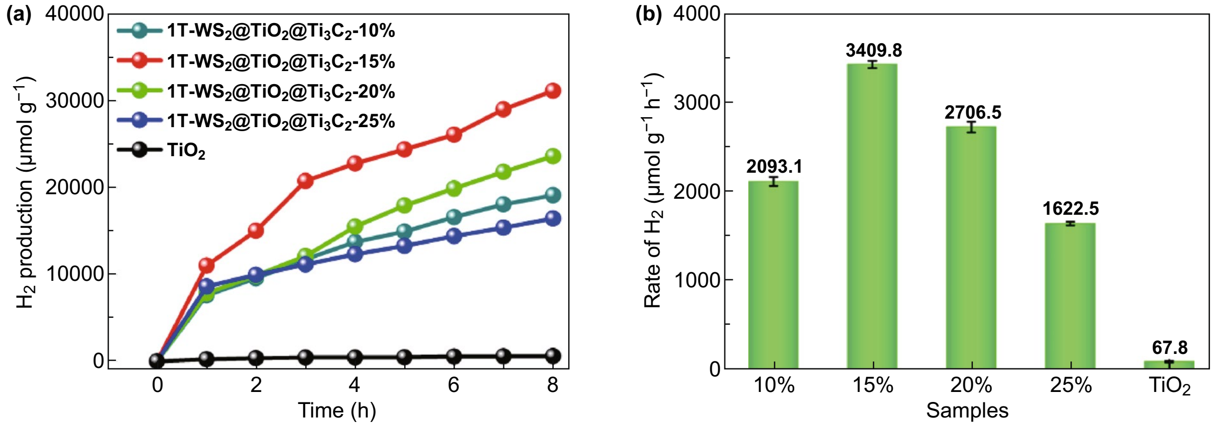

Fig. 6 **a** Photocatalytic H_2 production and **b** rate of the samples under simulated sunlight illumination

Besides, we evaluate the apparent quantum efficiency (AQE) of photocatalysts under the same light source. Table S2 displays the comparison of AQE values of TiO_2 NSs and 1T-WS_2@TiO_2@Ti_3C_2 composites with different WS_2 ratios (10, 15, 20, and 25 wt%): 0.049% (TiO_2 NSs) < 1.173% (1T-WS_2@TiO_2@Ti_3C_2-25 wt%) < 1.513% (1T-WS_2@TiO_2@Ti_3C_2-10 wt%) < 1.956% (1T-WS_2@TiO_2@Ti_3C_2-20 wt%) < 2.464% (1T-WS_2@TiO_2@Ti_3C_2-15 wt%), which is in accordance with photocatalytic H_2 evolution performance. Moreover, we conduct stability of 1T-WS_2@TiO_2@Ti_3C_2 composites (15 wt% WS_2) for 24 h (Fig. S7). No noticeable H_2 production decrease is detected after 3 cycles (24 h). SEM images (Fig. S8) and XRD pattern (Fig. S9) of 1T-WS_2@TiO_2@Ti_3C_2 composites after 3 cycles display no evident difference compared with fresh samples. The results further demonstrate that 1T-WS_2@TiO_2@Ti_3C_2 composites can act as a favorable photocatalyst for H_2 production. We also delaminated the multilayered Ti_3C_2 MXenes to get monolayered Ti_3C_2 nanosheets (Fig. S10). The XRD pattern of TiO_2@Ti_3C_2 (monolayer) does not detect the diffraction peak of Ti_3C_2 (Fig. S10a). Since Ti_3C_2 monolayer is in full contact with the reaction solution, all Ti_3C_2 may be converted into TiO_2 under the same experimental conditions. As shown in Fig. S10b, 1T-WS_2@Ti_3C_2@Ti_3C_2 (monolayer) presents worse photocatalytic H_2 production activity than that of 1T-WS_2@TiO_2@Ti_3C_2 (multilayer), which demonstrates that the lack of Ti_3C_2 by oxidation in 1T-WS_2@Ti_3C_2@Ti_3C_2 (monolayer) greatly affects the photocatalytic H_2 production. Furthermore, changing the ratio between Ti_3C_2 and TiO_2 also affecting the photocatalytic performance of 1T-WS_2@TiO_2@Ti_3C_2 composites (Fig. S11). Compared with in situ loading of TiO_2 nanosheets (Fig. S12), foreign titanium sources do not improve the photocatalytic performance of 1T-WS_2@TiO_2@Ti_3C_2 composites, which may be caused by the non-close contact between TiO_2 and Ti_3C_2 caused by the foreign titanium sources.

The introduction of Ti_3C_2 MXene and 1T-WS_2 in 1T-WS_2@TiO_2@Ti_3C_2 composites would be believed to influence photoinduced carrier separation, which could be characterized by steady and time-resolved PL spectroscopy (Fig. 7). As illustrated in Fig. 7a, TiO_2 NSs possess a high PL peak, resulting in the quick photoinduced carrier recombination. When Ti_3C_2 MXene and 1T-WS_2 are incorporated, the PL peak is significantly reduced (Fig. 7a). Evidently, the photoinduced carrier recombination of TiO_2 is hindered by migrating electrons to Ti_3C_2 and 1T-WS_2 as electron acceptors [44]. An increased lifetime of charge carriers is also detected by loading Ti_3C_2 MXene and 1T-WS_2 (Fig. 7b). The intensity-average lifetimes (τ) of TiO_2 NSs are 0.1138 ns, much shorter than that of 1T-WS_2@TiO_2@Ti_3C_2 composites (1.2750 ns). The increased carrier lifetime of 1T-WS_2@TiO_2@Ti_3C_2 composites is beneficial for enhanced carrier separation efficiency.

The photocurrent responses of photocatalysts were prompt by some on–off cycles under light illumination (Fig. 8a). All of samples present reversible photocurrent responses on each irradiation. The photocurrent intensity of 1T-WS_2@TiO_2@Ti_3C_2 composites is much higher than that of pure TiO_2 NSs, which is due to Ti_3C_2 and 1T-WS_2 as co-catalysts more effectively receiving photoexcited electrons of TiO_2. The 1T-WS_2@TiO_2@Ti_3C_2 composites

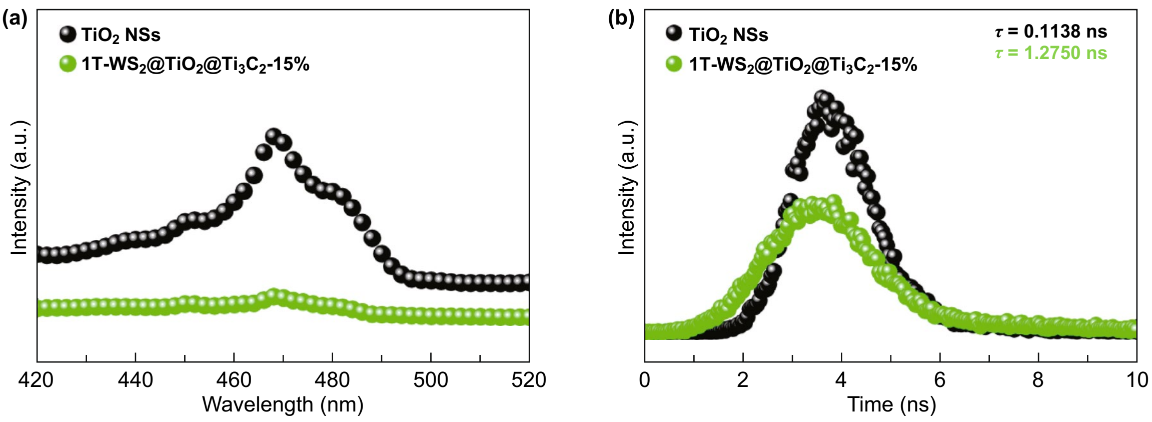

Fig. 7 **a** Steady and **b** time-resolved PL spectra of TiO_2 NSs and 1T-WS_2@TiO_2@Ti_3C_2 composites (15 wt% WS_2), $\lambda_{ex} = 325$ nm

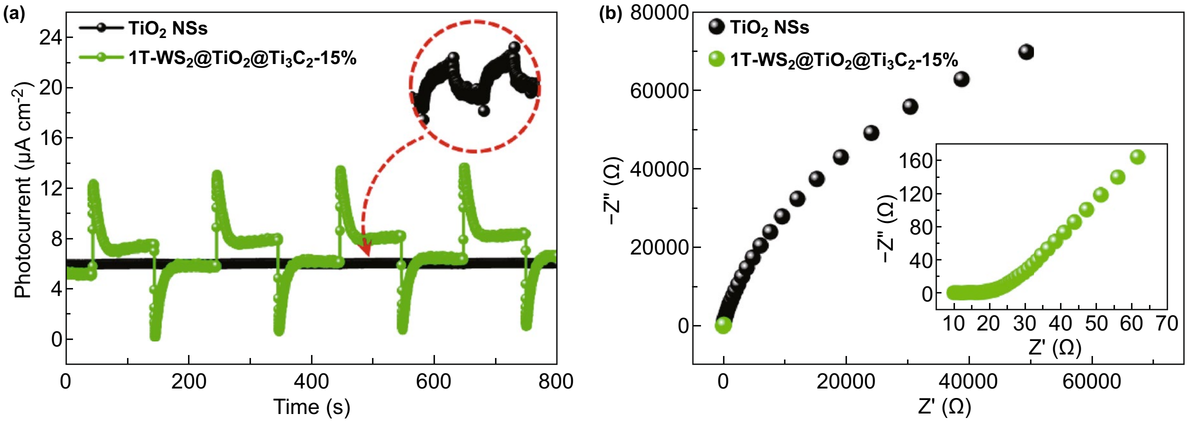

Fig. 8 **a** Transient photocurrent responses and **b** EIS of TiO_2 NSs and 1T-WS_2@TiO_2@Ti_3C_2 composites (15 wt% WS_2)

(Fig. 8b) exhibit a smaller arc radius compared with TiO_2 NSs under light irradiation, suggesting that the 1T-WS_2@TiO_2@Ti_3C_2 composite presents smaller charge transfer resistance, finally causing higher photoexcited carrier transfer and separation efficiency [45].

As shown in Scheme 2, under light irradiation, TiO_2 NSs can be excited to produce electrons and holes. The majority of photoexcited electrons in conduction band (CB) of TiO_2 could instantly migrate to metallic Ti_3C_2 MXene and 1T-WS_2 through the interface. As the photoelectron receivers, Ti_3C_2 MXene and 1T-WS_2 serves as active sites for H_2 production [46, 47]. Meanwhile, the holes in the valence band (VB) of TiO_2 are consumed by the sacrificial reagents. Consequently, the photoexcited carriers are efficiently transferred and separated with the assistance of double co-catalysts Ti_3C_2 and 1T-WS_2.

4 Conclusions

In conclusion, an effective 1T-WS_2@TiO_2@Ti_3C_2 composite photocatalyst is successfully prepared. The development of TiO_2 NSs on Ti_3C_2 MXenes and 1T-WS_2 nanoparticles uniformly distributing on TiO_2@Ti_3C_2 composite is the design concept. The obtained 1T-WS_2@TiO_2@Ti_3C_2 composite with 15 wt% WS_2 loading displays excellent photocatalytic H_2 production performance (3409.8 μmol g^{-1} h^{-1}), nearly 50 times higher than that of pure TiO_2 NSs. The excellent H_2 evolution performance of 1T-WS_2@TiO_2@Ti_3C_2 composites is ascribed to the following reasons: (1) The introduction of 1T-WS_2 nanoparticles induces enhanced BET surface area and more active sites; (2) Both Ti_3C_2 MXene and 1T-WS_2 possess extraordinary conductivity, which greatly enhance the electron transfer ability and thus achieve highly efficient spatial charge separation.

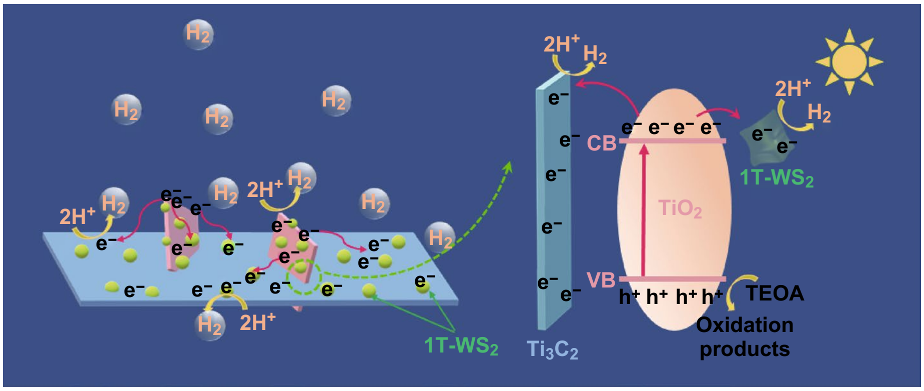

Scheme 2 Schematic photocatalytic mechanism of 1T-WS_2@TiO_2@Ti_3C_2 composites

Acknowledgements The authors are thankful for fundings from the National Natural Science Foundation of China (Nos. 51872173 and 51772167), Taishan Scholarship of Young Scholars (No. tsqn201812068), Natural Science Foundation of Shandong Province (No. ZR2017JL020), Taishan Scholarship of Climbing Plan (No. tspd20161006), and Key Research and Development Program of Shandong Province (No. 2018GGX102028).

Electronic supplementary material The online version of this article (https://doi.org/10.1007/s40820-019-0339-0) contains supplementary material, which is available to authorized users.

References

1. S.W. Boettcher, E.L. Warren, M.C. Putnam, E.A. Santori, D.T. Evans et al., Photoelectrochemical hydrogen evolution using Si microwire arrays. J. Am. Chem. Soc. **133**, 1216–1219 (2011). https://doi.org/10.1021/ja108801m
2. J. Choi, S.Y. Ryu, W. Balcerski, T.K. Lee, M.R. Hoffmann, Photocatalytic production of hydrogen on Ni/NiO/$KNbO_3$/CdS nanocomposites using visible light. J. Mater. Chem. **18**, 2371–2378 (2008). https://doi.org/10.1039/B718535A
3. M.R. Gholipour, C.T. Dinh, F. Béland, T.O. Do, Nanocomposite heterojunctions as sunlight-driven photocatalysts for hydrogen production from water splitting. Nanoscale **7**, 8187–8208 (2015). https://doi.org/10.1039/C4NR07224C
4. Z. Li, B. Tian, W. Zhen, Y. Wu, G. Lu, Inhibition of hydrogen and oxygen recombination using oxygen transfer reagent hemin chloride in Pt/TiO_2 dispersion for photocatalytic hydrogen generation. Appl. Catal. B-Environ. **203**, 408–415 (2017). https://doi.org/10.1016/j.apcatb.2016.10.049
5. Z. Liang, X. Bai, P. Hao, Y. Guo, Y. Xue, J. Tian, H. Cui, Full solar spectrum photocatalytic oxygen evolution by carbon-coated TiO_2 hierarchical nanotubes. Appl. Catal. B **243**, 711–720 (2019). https://doi.org/10.1016/j.apcatb.2018.11.017
6. X. Zhang, Y. Wang, B. Liu, Y. Sang, L. Hong, Heterostructures construction on TiO_2 nanobelts: a powerful tool for building high-performance photocatalysts. Appl. Catal. B **202**, 620–641 (2017). https://doi.org/10.1016/j.apcatb.2016.09.068
7. Y. Cao, Y. Saygili, A. Ummadisingu, J.L. Teuscher, J. Luo, N. Pellet, F. Giordano, S.M. Zakeeruddin, J.E. Moser, M. Freitag, 11% efficiency solid-state dye-sensitized solar cells with copper (II/I) hole transport materials. Nat. Commun. **8**, 15390 (2017). https://doi.org/10.1038/ncomms15390
8. N. Michael, Alkaline earth metal oxide nanocluster modification of rutile TiO_2 (110) promotes water activation and CO_2 chemisorption. J. Mater. Chem. A **6**, 9451–9466 (2018). https://doi.org/10.1039/C8TA01789A
9. J. Jiao, Y. Wei, Y. Zhao, Z. Zhao, A. Duan et al., AuPd/3DOM-TiO_2 catalysts for photocatalytic reduction of CO_2: high efficient separation of photogenerated charge carriers. Appl. Catal. B **209**, 228–239 (2017). https://doi.org/10.1016/j.apcatb.2017.02.076
10. S. Ma, Y. Deng, J. Xie, K. He, W. Liu, X. Chen, X. Li, Noble-metal-free Ni_3C cocatalysts decorated CdS nanosheets for high-efficiency visible-light-driven photocatalytic H_2 evolution. Appl. Catal. B **227**, 218–228 (2018). https://doi.org/10.1016/j.apcatb.2018.01.031
11. Y.J. Yuan, D. Chen, J. Zhong, L.X. Yang, J. Wang et al., Interface engineering of a noble-metal-free 2D-2D MoS_2/Cu-$ZnIn_2S_4$ photocatalyst for enhanced photocatalytic H_2 production. J. Mater. Chem. A **5**, 15771–15779 (2017). https://doi.org/10.1039/C7TA04410K
12. Y.J. Yuan, H.W. Lu, Z.T. Yu, Z.G. Zou, Noble-metal-free molybdenum disulfide cocatalyst for photocatalytic hydrogen production. Chemsuschem **8**, 4113–4127 (2016). https://doi.org/10.1002/cssc.201501203
13. Y. Sun, X. Meng, Y. Dall'Agnese, C. Dall'Agnese, S. Duan, Y. Gao, G. Chen, X.F. Wang, 2D MXenes as co-catalysts in photocatalysis: synthetic methods. Nano-Micro Lett. **11**, 79 (2019). https://doi.org/10.1007/s40820-019-0309-6
14. M. Naguib, V.N. Mochalin, M.W. Barsoum, Y. Gogotsi, 25th anniversary article: MXenes: a new family of two-dimensional materials. Adv. Mater. **26**, 992–1005 (2014). https://doi.org/10.1002/adma.201304138
15. Z. Li, F. Wu, J. Yu, Q. Deng, F. Zhang, W. Guan, Titanium carbide ($Ti_3C_2T_x$) MXene: a novel precursor to amphiphilic carbide-derived graphene quantum dots for fluorescent ink, light-emitting composite and bioimaging. Carbon **118**, 50–57 (2017). https://doi.org/10.1016/j.carbon.2017.03.023
16. X. Xie, M.Q. Zhao, B. Anasori, K. Maleski, C.E. Ren, J. Li, B.W. Byles, E. Pomerantseva, G. Wang, Y. Gogotsi, Porous heterostructured MXene/carbon nanotube composite paper with high volumetric capacity for sodium-based energy storage devices. Nano Energy **26**, 513–523 (2016). https://doi.org/10.1016/j.nanoen.2016.06.005
17. Y. Li, X. Deng, J. Tian, Z. Liang, H. Cui, Ti_3C_2 MXene-derived Ti_3C_2/TiO_2 nanoflowers for noble-metal-free photocatalytic overall water splitting. Appl. Mater. Today **13**, 217–227 (2018). https://doi.org/10.1016/j.apmt.2018.09.004
18. J. Pang, R.G. Mendes, A. Bachmatiuk, L. Zhao, H.Q. Ta et al., Applications of 2D MXenes in energy conversion and storage systems. Chem. Soc. Rev. **48**, 72–133 (2019). https://doi.org/10.1039/C8CS00324F

19. J. Yi, X. She, Y. Song, M. Mao, K. Xia et al., Solvothermal synthesis of metallic 1T-WS_2: a supporting co-catalyst on carbon nitride nanosheets toward photocatalytic hydrogen evolution. Chem. Eng. J. **335**, 282–289 (2018). https://doi.org/10.1016/j.cej.2017.10.125
20. J.M. Woods, Y. Jung, Y. Xie, W. Liu, Y. Liu, H. Wang, J.J. Cha, One-step synthesis of MoS_2/WS_2 layered heterostructures and catalytic activity of defective transition metal dichalcogenide films. ACS Nano **10**, 2004–2009 (2016). https://doi.org/10.1021/acsnano.5b06126
21. X. Tong, Y. Qi, J. Chen, N. Wang, Q. Xu, Supercritical CO_2-assisted reverse-micelle-induced solution-phase fabrication of two-dimensional metallic 1T-MoS_2 and 1T-WS_2. ChemNanoMat **3**, 466–471 (2017). https://doi.org/10.1002/cnma.201700011
22. M. Piao, J. Chu, X. Wang, Y. Chi, H. Zhang, C. Li, H. Shi, M.K. Joo, Hydrothermal synthesis of stable metallic 1T phase WS_2 nanosheets for thermoelectric application. Nanotechnology **29**, 025705 (2017). https://doi.org/10.1088/1361-6528/aa9bfe
23. Q. Liu, X. Li, Z. Xiao, Y. Zhou, H. Chen et al., Stable metallic 1T-WS2 nanoribbons intercalated with ammonia ions: the correlation between structure and electrical/optical properties. Adv. Mater. **27**, 4837–4844 (2015). https://doi.org/10.1002/adma.201502134
24. U. Maitra, U. Gupta, M. De, R. Datta, A. Govindaraj, C.N. Rao, Highly effective visible-light-induced H_2 generation by single-layer 1T-MoS_2 and a nanocomposite of few-layer 2H-MoS_2 with heavily nitrogenated graphene. Angew. Chem. Int. Ed. **52**, 13057–13061 (2013). https://doi.org/10.1002/anie.201306918
25. H. Yu, P. Xiao, P. Wang, J. Yu, Amorphous molybdenum sulfide as highly efficient electron-cocatalyst for enhanced photocatalytic H_2 evolution. Appl. Catal. B **193**, 217–225 (2016). https://doi.org/10.1016/j.apcatb.2016.04.028
26. X.B. Li, Y.J. Gao, H.L. Wu, Y. Wang, Q. Guo et al., Assembling metallic 1T-MoS_2 nanosheets with inorganic-ligand stabilized quantum dots for exceptional solar hydrogen evolution. Chem. Commun. **53**, 5606–5609 (2017). https://doi.org/10.1039/C7CC02366A
27. Y. Li, Z. Yin, G. Ji, Z. Liang, Y. Xue, Y. Guo, J. Tian, X. Wang, H. Cui, 2D/2D/2D heterojunction of Ti_3C_2 MXene/MoS_2 nanosheets/TiO_2 nanosheets with exposed (001) facets toward enhanced photocatalytic hydrogen production activity. Appl. Catal. B **246**, 12–20 (2019). https://doi.org/10.1016/j.apcatb.2019.01.051
28. M.A. Lukowski, A.S. Daniel, F. Meng, A. Forticaux, L. Li, S. Jin, Enhanced hydrogen evolution catalysis from chemically exfoliated metallic MoS_2 nanosheets. J. Am. Chem. Soc. **135**, 10274–10277 (2013). https://doi.org/10.1021/ja404523s
29. M. Naguib, M. Kurtoglu, V. Presser, J. Lu, J. Niu, H. Min, L. Hultman, Y. Gogotsi, M.W. Barsoum, Two-dimensional nanocrystals: two-dimensional nanocrystals produced by exfoliation of Ti3AlC2. Adv. Mater. **37**, 4207 (2011). https://doi.org/10.1002/adma.201190147
30. C.C.M. Martinez, A. Ambrosi, A.Y.S. Eng, Z. Sofer, M. Pumera, Metallic 1T-WS2 for selective impedimetric vapor sensing. Adv. Funct. Mater. **25**, 5611–5616 (2015). https://doi.org/10.1002/adfm.201502223
31. J. Tian, X. Hu, N. Wei, Y. Zhou, X. Xu, H. Cui, H. Liu, RuO_2/TiO_2 nanobelt heterostructures with enhanced photocatalytic activity and gas-phase selective oxidation of benzyl alcohol. Sol. Energ. Mat. Sol. C **151**, 7–13 (2016). https://doi.org/10.1016/j.solmat.2016.02.017
32. X. Hu, S. Lu, J. Tian, N. Wei, X. Song, X. Wang, H. Cui, The selective deposition of MoS_2 nanosheets onto (101) facets of TiO_2 nanosheets with exposed (001) facets and their enhanced photocatalytic H_2 production. Appl. Catal. B **241**, 329–337 (2019). https://doi.org/10.1016/j.apcatb.2018.09.051
33. P. Lian, Y. Dong, Z. Wu, S. Zheng, X. Wang, S. Wang, C. Sun, J. Qin, X. Shi, X. Bao, Alkalized Ti_3C_2 MXene nanoribbons with expanded interlayer spacing for high-capacity sodium and potassium ion batteries. Nano Energy **40**, 1–8 (2017). https://doi.org/10.1016/j.nanoen.2017.08.002
34. T.A.J. Loh, D.H.C. Chua, Origin of hybrid 1T- and 2H-WS_2 ultrathin layers by pulsed laser deposition. J. Phys. Chem. C **49**, 27496–27504 (2015). https://doi.org/10.1021/acs.jpcc.5b09277
35. B. Mahler, V. Hoepfner, K. Liao, G.A. Ozin, Colloidal synthesis of 1T-WS_2 and 2H-WS_2 nanosheets: aplications for photocatalytic hydrogen evolution. J. Am. Chem. Soc. **136**, 14121–14127 (2014). https://doi.org/10.1021/ja506261t
36. F. Yang, Z. Ning, H. Liu, Fractal characteristics of shales from a shale gas reservoir in the Sichuan Basin. China Fuel **115**, 378–384 (2014). https://doi.org/10.1016/j.fuel.2013.07.040
37. Y. Cui, G. Zhang, Z. Lin, X. Wang, Condensed and low-defected graphitic carbon nitride with enhanced photocatalytic hydrogen evolution under visible light irradiation. Appl. Catal. B **181**, 413–419 (2016). https://doi.org/10.1016/j.apcatb.2015.08.018
38. H. Yang, J. Tian, Y. Bo, Y. Zhou, X. Wang, H. Cui, Visible photocatalytic and photoelectrochemical activities of TiO_2 nanobelts modified by In_2O_3 nanoparticles. J. Colloid Interf. Sci. **487**, 258–265 (2017). https://doi.org/10.1016/j.jcis.2016.10.051
39. J. Ran, G. Gao, F. Li, T. Ma, A. Du, S. Qiao, Ti_3C_2 MXene co-catalyst on metal sulfide photo-absorbers for enhanced visible-light photocatalytic hydrogen production. Nat. Commun. **8**, 13907 (2017). https://doi.org/10.1038/ncomms13907
40. L. Yao, N. Zhang, Y. Wang, Y. Ni, Facile formation of 2D $Co_2P@Co_3O_4$ microsheets through in situ toptactic conversion and surface corrosion: bifunctional electrocatalysts towards overall water splitting. J. Power Sources **374**, 142–148 (2018). https://doi.org/10.1016/j.jpowsour.2017.11.028
41. A.N. Enyashin, A.L. Ivanovskii, Structural and electronic properties and stability of MXenes Ti_2C and Ti_3C_2 functionalized by methoxy groups. J. Phys. Chem. C **117**, 13637–13643 (2013). https://doi.org/10.1021/jp401820b
42. T.A.J. Loh, M. Tanemura, D.H.C. Chua, Ultrathin MoS_2 and WS_2 layers on silver nano-tips as electron emitters. Appl. Phys. Lett. **109**, 133102 (2016). https://doi.org/10.1063/1.4963260

43. H.E. Kim, J. Lee, H. Lee, C. Lee, Synergistic effects of TiO_2 photocatalysis in combination with fenton-like reactions on oxidation of organic compounds at circumneutral pH. Appl. Catal. B **116**, 219–224 (2012). https://doi.org/10.1016/j.apcatb.2011.12.027

44. M. Schvartzman, V. Sidorov, D. Ritter, Y. Paz, Surface passivation of (100) InP by organic thiols and polyimide as characterized by steady-state photoluminescence. Semicond. Sci. Technol. **16**, 68–71 (2001). https://doi.org/10.1088/0268-1242/16/10/103

45. Y. Liu, W. Wang, Y. Wang, X. Peng, Homogeneously assembling like-charged WS_2 and GO nanosheets lamellar composite films by filtration for highly efficient lithium ion batteries. Nano Energy **7**, 25–32 (2014). https://doi.org/10.1016/j.nanoen.2014.04.018

46. A. Manikandan, P.R. Ilango, C.W. Chen, Y.C. Wang, Y.C. Shih et al., A superior dye adsorbent towards the hydrogen evolution reaction combining active sites and phase-engineering of (1T/2H) MoS_2/α-MoO_3 hybrid heterostructured nanoflowers. J. Mater. Chem. A **6**, 15320 (2018). https://doi.org/10.1039/C8TA02496K

47. X. An, W. Wang, J. Wang, H. Duan, J. Shi, X. Yu, The synergetic effects of Ti_3C_2 MXene and Pt as co-catalysts for highly efficient photocatalytic hydrogen evolution over g-C_3N_4. Phys. Chem. Chem. Phys. **20**, 11405–11411 (2018). https://doi.org/10.1039/C8CP01123K